



TITLE:

Molecular Dynamics Analyses of Deformation Behavior of Long-Period-Stacking-Ordered Structures

AUTHOR(S):

Matsumoto, Ryosuke; Uranagase, Masayuki;
Miyazaki, Noriyuki

CITATION:

Matsumoto, Ryosuke ...[et al]. Molecular Dynamics Analyses of Deformation Behavior of Long-Period-Stacking-Ordered Structures. MATERIALS TRANSACTIONS 2013, 54(5): 686-692

ISSUE DATE:

2013

URL:

<http://hdl.handle.net/2433/194077>

RIGHT:

© 2013 The Mining and Materials Processing Institute of Japan

Molecular Dynamics Analyses of Deformation Behavior of Long-Period-Stacking-Ordered Structures

Ryosuke Matsumoto*, Masayuki Uranagase and Noriyuki Miyazaki

Department of Mechanical Engineering and Science, Graduate School of Engineering, Kyoto University, Kyoto 615-8246, Japan

Magnesium alloys containing long-period-stacking ordered (LPSO) phases have attracted considerable attention because they have been reported to exhibit excellent mechanical properties, including high strength and reasonable ductility. It is thought that the LPSO phase plays a critical role in producing these favorable mechanical properties. We analyze the deformation behavior of the LPSO phases with different stacking sequences using molecular dynamics simulations. To highlight the specific deformation behavior of the LPSO phases, we also perform deformation analyses of hexagonal-close-packed and face-centered-cubic (FCC) structures. We focus on the influence of the stacking order rather than the segregated atoms around the FCC-structured layers, and we model an LPSO structure by single element composition where the interatomic interaction is described by a smoothed Lennard-Jones potential. Our simulations indicate that an LPSO structure with a shorter stacking sequence tends to exhibit a higher compressive flow stress, because FCC-structured layers inhibit twinning deformations and non-basal slips. Kinking deformation is observed for an LPSO structure when both compression and shear deformation are present. It is shown that the first-order pyramidal- $(c + a)$ dislocation disarranges the stacking of an LPSO structure and leaves behind many lattice defects. In addition, those lattice defects activate numerous basal slips. Finally, basal dislocations arrange in a line and generate a misorientation angle. Furthermore, this angle originates the compressive deformation. We also observed some prismatic- (a) dislocations and cross slips to the basal plane. These results suggest the importance of non-basal slips for kinking deformation. [doi:10.2320/matertrans.MI201211]

(Received November 16, 2012; Accepted January 17, 2013; Published March 8, 2013)

Keywords: *molecular dynamics simulation, long-period-stacking-ordered structure, magnesium, kinking deformation, twinning deformation, dislocation, slip system*

1. Introduction

Because Magnesium (Mg) is the lightest structural metal, one would expect it to be used in various industrial applications. However, poor ductility and formability of regular Mg alloys have severely restricted their application potential. Recently developed Mg alloys that contain long-period-stacking-ordered (LPSO) phases, called Mg/LPSO two-phase alloys, have attracted considerable attention because they have been reported to exhibit excellent mechanical properties, including high yield stress and reasonable ductility.^{1–5)} For example, the Mg₉₇Zn₁Y₂ alloy with the Mg/LPSO two-phase structure fabricated by a non-equilibrium, rapid solidification process exhibits outstanding strength above 480 MPa and an elongation of 5 to 16%.¹⁾ It is thought that the LPSO phase plays a critical role in producing those excellent mechanical properties.⁵⁾ Some literatures show that the LPSO phases yield by kinking deformation under compression,^{6–8)} while conventional Mg alloys with a hexagonal close-packed (HCP) structure yield by twinning deformation. It is assumed that the kinking deformation is caused by the nucleation of many basal dislocation pairs and their motion in the opposite direction.⁹⁾ However, the detailed mechanisms of kinking deformation, e.g., dislocation source for the massive nucleation of basal dislocations, have not yet been clarified.

This study aims to obtain a microscopic picture of the kinking deformation of the LPSO phase and to reveal the relationship between kinking deformation and novel mechanical properties of LPSO alloys. We analyzed the deformation behavior of the LPSO phases with different stacking sequences using molecular dynamics (MD) simulations. To

highlight the specific deformation behavior of the LPSO phases, we also performed deformation analyses of HCP and face-centered-cubic (FCC) structures.

2. Calculation Method and Simulation Model

2.1 Modeling of LPSO phases

Various polytypes of LPSO structures such as 10H (hexagonal), 18R (rhombohedral), 14H and 24R have been observed.^{10,11)} A conventional Mg alloy has an HCP structure, and it has a two-layer periodic structure with basal plane stacking, generically expressed as AB, AB, AB, Conversely, for example, LPSO structures with 18R stacking have 18-layer periodic structures described as ABAB-ABCACACABCBCBC, ABABABCACACABCBCBC, Namely, LPSO structures have a long period stacking order with FCC-structured layers, i.e., ABC stacking, in HCP structures. Furthermore, LPSO structures also have a chemical order with segregation of added elements such as Zn and Y in FCC-structured layers.^{2,12–14)} Thus, the mechanical properties of LPSO structures are supposedly influenced by both their stacking order and chemical order.

Conversely, when performing MD simulations, the interatomic potentials of the constituent atoms and detailed atomic configuration of the initial structure are required. However, as far as is known, the interatomic potential of a ternary system that exhibits an LPSO phase is not available, and the development of a reliable potential is extremely difficult. Furthermore, detailed configurations of added elements in FCC-structured layers are known only for a limited number of systems.^{12–14)} For these reasons and for simplification, we focused on the influence of the stacking order rather than the chemical order, and we modeled LPSO structures by single element composition.

*Corresponding author, E-mail: matsumoto@solid.me.kyoto-u.ac.jp

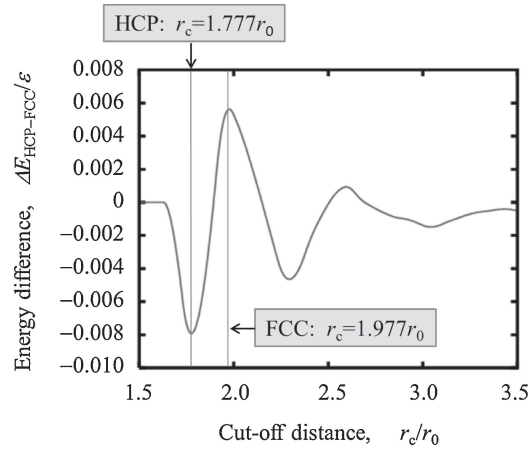


Fig. 1 Energy difference between HCP and FCC structures obtained by SLJ potential with different cut-off distances.

2.2 Interatomic potential

So far, some interatomic potentials of Mg have been proposed. They include the embedded-atom-method (EAM) potential by Sun *et al.*,¹⁵⁾ Pasianot and Savino,¹⁶⁾ and Liu *et al.*,¹⁷⁾ the modified EAM potential by Baskes *et al.*,¹⁸⁾ and the generalized EAM potential developed by Zhou *et al.*¹⁹⁾ Some of these potentials are applicable to deformation analyses of Mg lattices.²⁰⁾ However, if we employed an interatomic potential of Mg, FCC-structured layers in LPSO structures easily disappear under a small resolved shear stress along a basal-slip direction by generating partial dislocation pairs because an FCC structure (or a stacking fault in HCP structures) is not global stable.

In this study, we employ a smoothed Lennard-Jones (SLJ) potential, which is a modified form of the conventional 12-6-type Lennard-Jones (LJ) potential ϕ_{LJ} , to fulfill the continuity of the potential energy and its first derivative, $\phi'_{LJ} = d\phi_{LJ}/dr$, at the cut-off distance r_c .^{21,22)} The interaction energy between two atoms is expressed as follows.

$$\begin{aligned}\phi_{SLJ}(r) &= \phi_{LJ}(r) - \phi_{LJ}(r_c) - (r - r_c)\phi'_{LJ}(r_c) \\ \phi_{LJ}(r) &= \varepsilon \left\{ \left(\frac{r_0}{r} \right)^{12} - 2 \left(\frac{r_0}{r} \right)^6 \right\}.\end{aligned}\quad (1)$$

Here r is an interatomic distance, and ε and r_0 are potential parameters to determine the bonding energy and first-neighbor distance, respectively. The change of r_c alters the number of interacting atoms and the potential curve itself, and thus, the energy difference between HCP and FCC structures ($\Delta E_{HCP-FCC} = E_{HCP} - E_{FCC}$) varies depending on r_c . $\Delta E_{HCP-FCC}$ determines stability of structures. Figure 1 shows the relationship between $\Delta E_{HCP-FCC}/\varepsilon$ and r_c . Hence, we use $r_c = 1.740r_0$, where $\Delta E_{HCP-FCC}/\varepsilon$ is the smallest, for atoms in HCP layers at an initial state (initial HCP atoms), and $r_c = 1.936r_0$, where $\Delta E_{HCP-FCC}/\varepsilon$ is the largest, for atoms in FCC layers at an initial state (initial FCC atoms), and we obtain stable LPSO structures. ε is defined such that the maximum bonding energy between two atoms corresponds to that of the LJ potential of Mg (0.256×10^{-19} J (0.16 eV)).^{23,24)} We employed $r_0 = 0.3184$ nm, which is the first-neighbor distance of HCP-structured Mg,¹⁵⁾ for both the initial HCP and FCC atoms. We defined the potential

Table 1 Parameters for SLJ potential.

	First-neighbor distance, r_0/nm	Bonding energy, $\varepsilon/10^{-20}$ J/(eV)	Cut-off distance, r_c/r_0
HCP-HCP	0.3184	3.408 (0.2127)	1.740
FCC-FCC		3.001 (0.1873)	1.936
HCP-FCC		3.198 (0.1996)	1.838

parameters between the initial HCP and FCC atoms as follows.

$$\begin{aligned}r_{c_FCC-HCP} &= \frac{(r_{c_FCC} + r_{c_HCP})}{2} \\ \varepsilon_{FCC-HCP} &= \sqrt{\varepsilon_{FCC} \times \varepsilon_{HCP}}\end{aligned}\quad (2)$$

Table 1 shows the potential parameters. We employed the atomic mass of Mg ($m = 4.036 \times 10^{-26}$ kg) for all atoms.

Although a structural change occurs between the HCP structure and FCC structure, or FCC structure and HCP structure, during the deformation simulations, we do not change the potential parameters in accordance with the local structure, as is the case in conventional MD simulations, but use potential parameters for the initial structure. This is because it is thought that the FCC-structured layers in LPSO structures are stabilized by added elements such as Zn and Y, and those atoms rarely diffuse during deformation.

The energy difference between an HCP and FCC structure — $\Delta E_{HCP-FCC}$ — is -2.724×10^{-22} J/atom (-0.0017 eV/atom) for the initial HCP atom and 1.602×10^{-22} J/atom (0.0010 eV/atom) for the initial FCC atom, respectively. These values are almost 1/10 of the value for the actual Mg atom (2.083×10^{-21} J/atom (0.013 eV/atom)¹⁵⁾).

2.3 Initial structures

We analyzed the deformation behavior of the LPSO phases with different stacking sequences, i.e., 10H, 18R, 14H and 24R, using MD simulations. The interlayer spacing between two FCC-structured layers is the closest in 10H (3 HCP-structured layers), and becomes sparser in the order corresponding to 18R (4 HCP-structured layers), 14H (5 HCP-structured layers) and 24R (6 HCP-structured layers). To highlight the specific deformation behavior of the LPSO phases, we also performed deformation analyses of HCP and FCC structures.

For the construction of LPSO-structure and HCP-structure models, we periodically arranged those unit structures¹¹⁾ whose basal plane is parallel to the y - z plane and a basal slip direction is along the y direction (i.e., $[0001]$ (or c -axis) is along the x direction, $[11\bar{2}0]$ (or a -axis) is along the y direction, and $[\bar{1}100]$ is along the z direction). For the FCC-structure model, we set a slip plane (111) parallel to the y - z plane and a slip direction $[\bar{1}10]$ along the y direction. Figure 2 shows the simulation model with an LPSO structure with 18R stacking. All simulation models have dimensions $l_x \approx 18.1$ nm, $l_y \approx 31.8$ nm and $l_z \approx 18.7$ nm, and they are constructed from about 490000 atoms. No periodic boundary condition is applied, and thus, the calculation models have a square-pillar shape.

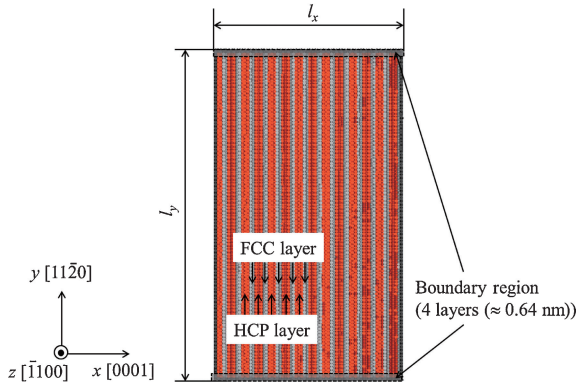


Fig. 2 Initial structure (Three-dimensional LPSO model with 18R stacking order).

2.4 Relaxation and deformation conditions

The boundary regions were defined as the upper and bottom four layers along the y direction as shown in Fig. 2, and the x and y directional motions of the atoms in the boundary regions were constrained. The time integration was performed by the velocity Verlet algorithm using a time step $\Delta t = 2$ fs. The temperature was controlled at 300 K by the velocity scaling method in all MD simulations.

We performed relaxation during 63 ps under the fixed boundary. During the relaxation, the atomic velocity of all atoms was reset every 6 ps to remove vibration, and the model sizes were scaled such that the average stresses were reduced to zero.

We defined the deformation direction using the parameters $\alpha = -\dot{\gamma}_{xy}/\dot{\epsilon}_{yy}$, where $\dot{\gamma}_{xy}$ and $\dot{\epsilon}_{yy}$ are the shear and tensile strain rates, respectively. Following the relaxation, the simulation models were deformed by giving all atoms x and y directional displacements at each time step, which correspond to $\alpha = 0$ or 4 under the constant equivalent strain rate $\dot{\epsilon}^{eq} = 10^8$ or 10^9 s $^{-1}$.

3. Results and Discussion

3.1 Overview of deformation behavior

In this section, we give brief overview of simulations results, and classify deformation behavior into four typical deformation modes. The detailed deformation process of each deformation mode and relation with stress–strain curve are given in the following sections.

Figure 3 shows the stress–strain curves under the equivalent strain rate $\dot{\epsilon}^{eq} = 10^8$ s $^{-1}$. Although a quantitative discussion is difficult because of the extremely high strain rates employed in the MD simulations and the absence of initial lattice-defect conditions, we can qualitatively discuss the influence of FCC-structured layers on the deformation resistance. It is clearly shown that a gradual stress change with typical serration is observed in the stress–strain curves of LPSO structures (especially 10H and 14H in Fig. 3(a) and 10H, 18R and 14H in Fig. 3(c)). Conversely, the compressive stress of the HCP structure sharply decreases to small magnitude after yielding and keeps small order. A rapid oscillation of stress is also observed for the HCP structure under $\alpha = 4$ (Figs. 3(b) and 3(c)). This is because FCC-structured layers inhibit twinning deformations, and LPSO

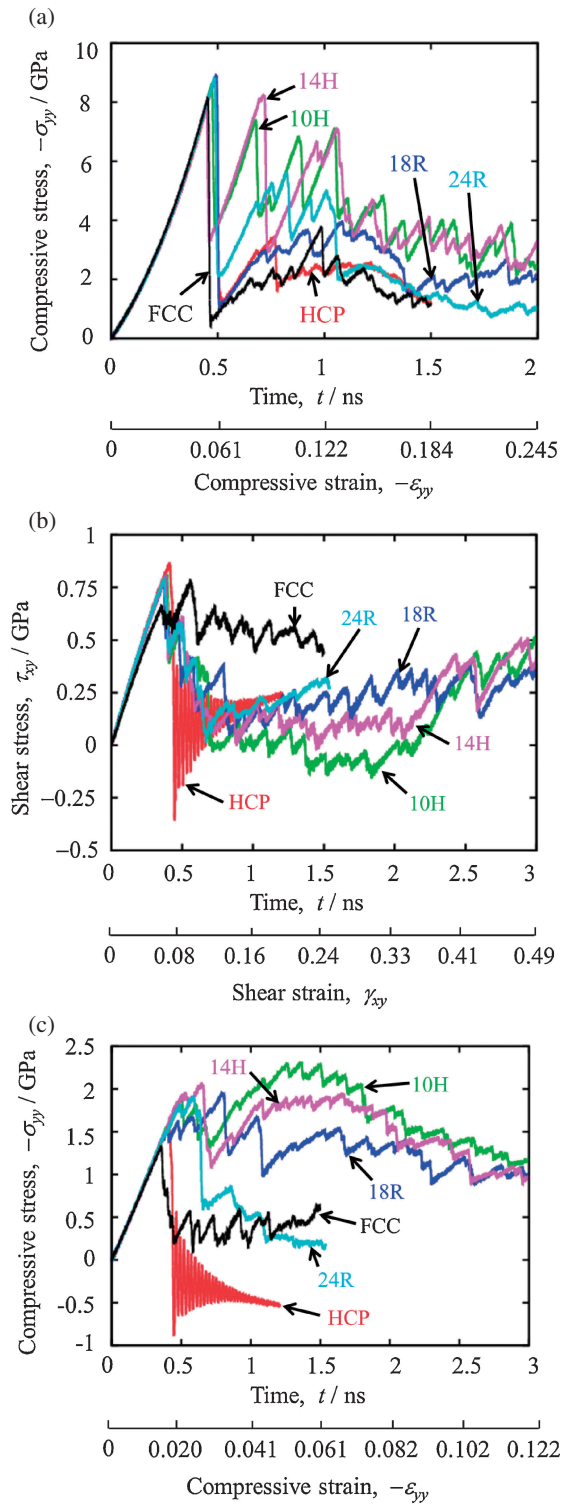


Fig. 3 Comparison of stress–strain curves under equivalent strain rate of $\dot{\epsilon}^{eq} = 1 \times 10^8$ s $^{-1}$ ((a) Compressive stress–strain relation under $\alpha = 0$, (b) Shear stress–strain relation under $\alpha = 4$, and (c) Compressive stress–strain relation under $\alpha = 4$).

structures mainly exhibit kinking deformation or deformation by non-basal dislocations, while the HCP structure deforms by the catastrophic propagation of twinning deformation, as shown later.

Figure 4 presents the typical deformation state at each deformation condition in tabular form. To visualize the atomic structure, we first use common neighbor analysis²⁵⁾ to

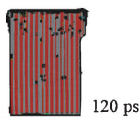
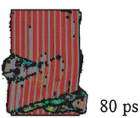
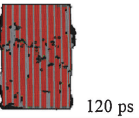
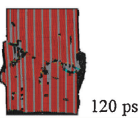
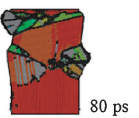
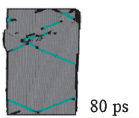
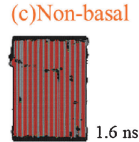
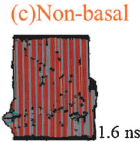
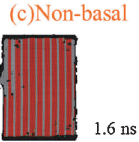
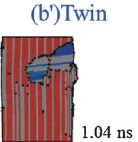
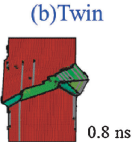
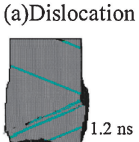
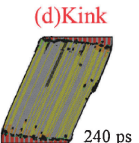
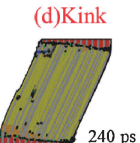
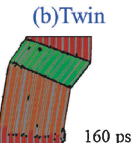
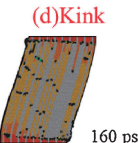
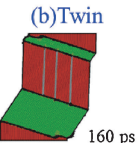
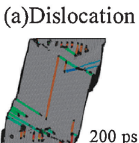
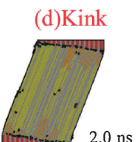
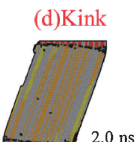
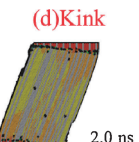
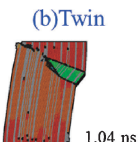
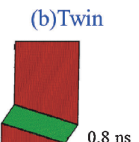
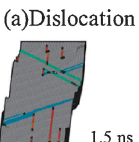
α	Strain rate, $\dot{\epsilon}^{\text{ep}} / \text{s}^{-1}$	LPSO (10H)	LPSO (18R)	LPSO (14H)	LPSO (24R)	HCP	FCC
0	10^9	(c)Non-basal  120 ps	(b)Twin  80 ps	(c)Non-basal  120 ps	(c)Non-basal  120 ps	(b)Twin  80 ps	(a)Dislocation  80 ps
	10^8	(c)Non-basal  1.6 ns	(c)Non-basal  1.6 ns	(c)Non-basal  1.6 ns	(b')Twin  1.04 ns	(b)Twin  0.8 ns	(a)Dislocation  1.2 ns
4	10^9	(d)Kink  240 ps	(d)Kink  240 ps	(b)Twin  160 ps	(d)Kink  160 ps	(b)Twin  160 ps	(a)Dislocation  200 ps
	10^8	(d)Kink  2.0 ns	(d)Kink  2.0 ns	(d)Kink  2.0 ns	(b)Twin  1.04 ns	(b)Twin  0.8 ns	(a)Dislocation  1.5 ns

Fig. 4 Comparison of deformation behavior under various deformation conditions: Figures show a typical deformation state at the mid plane ($z = l_z/2$) at each deformation condition. Atoms shown in black and gray are defect atoms (other than FCC- or HCP-structured atoms) and FCC-structured atoms, respectively. HCP-structured atoms are colored according to local c -axis direction, i.e., red, green and blue indicate the angle between the projection vector of the c -axis on the x - y plane and x directions are 0° , 45° , 90° , respectively and continuous RGB coloring is used for intermediate angles.

categorize the atoms according to the local structure into (i) HCP-structured atoms, (ii) FCC-structured atoms, and (iii) defect atoms that have a structure other than that of the HCP and FCC structures. For (i) HCP-structured atoms, we defined the c -axis ([0001]) using the positional relationship of six second neighbor atoms and estimated the angle φ between the projection vector of the c -axis on the x - y plane and x direction. Next, the HCP-structured atoms are colored according to $|\varphi|$, i.e., red, green and blue indicates $|\varphi| = 0$, 45° and 90° , respectively, and continuous RGB coloring is used for intermediate angles. (ii) FCC-structured atoms and (iii) defect atoms are shown in gray and black color, respectively. In Fig. 4, we find four typical deformation modes; i.e., (a) dislocation-based deformation in FCC structures (indicated as “(a) Dislocation” in the figure), (b) twinning deformation mainly observed in HCP structures (indicated as “(b) Twin” or “(b') Twin”), (c) deformation mainly caused by non-basal dislocations in LPSO structures under pure compression ($\alpha = 0$) (indicated as “(c) Non-basal”), and (d) kinking deformation observed in LPSO structures under compression plus shear deformation ($\alpha = 4$) (indicated as “(d) Kink”). The deformation behavior of FCC structures has been sufficiently studied in the past. Here we will focus on (b) twinning deformation, (c) deformation by non-basal dislocations, and (d) kinking deformation. In the following sections, we discuss the deformation processes and relationships with the stress–strain curve.

3.2 Twinning deformation

Figure 5 shows the typical twinning deformation process. For HCP structures, twinning deformation was observed for

all deformation conditions including the boundary condition where the resolved shear stress in the basal-slip direction became large ($\alpha = 4$), and the propagation was catastrophically fast. It takes only a few picoseconds to cross the simulation model (Figs. 5(a) and 5(b)), and the corresponding stress drop is observed in the stress–strain curves (~ 0.77 ns in Fig. 3(a) and ~ 0.43 ns in Figs. 3(b) and 3(c)). Because the twin boundaries migrate easily, the stress–strain curves oscillate around a small magnitude of stress when the twinning band completely crosses the model as shown in Fig. 5(b)(ii). Twinning deformation was also observed in the deformed LPSO structures under some deformation conditions. The initiation condition of twinning deformation in LPSO structures is not clear from the present simulations. However, it is confirmed that twinning deformation tends to be inhibited in an LPSO structures with a higher density of FCC-structured layers (e.g., no case for 10H stacking and two cases for 24R stacking as shown in Fig. 4). Figure 5(c) shows the twinning deformation that occurred in the LPSO structure with 24R stacking under $\alpha = 4$ and $\dot{\epsilon}^{\text{eq}} = 10^8 \text{ s}^{-1}$. The leading edge of the twinning deformation was frequently arrested at FCC-structured layers, and the propagation was much slower than that in the HCP structure. Furthermore, after the twinning region crossed the whole model, the migration of twin boundaries in the LPSO structures was also slower than that in the HCP structure. These results indicate that FCC-structured layers impede twinning deformations (both propagation and migration of twin boundary). The twinning system was detected except for the LPSO structure with 24R stacking that was deformed under $\alpha = 0$ and $\dot{\epsilon}^{\text{eq}} = 10^8$ (indicated as “(b') Twin” in

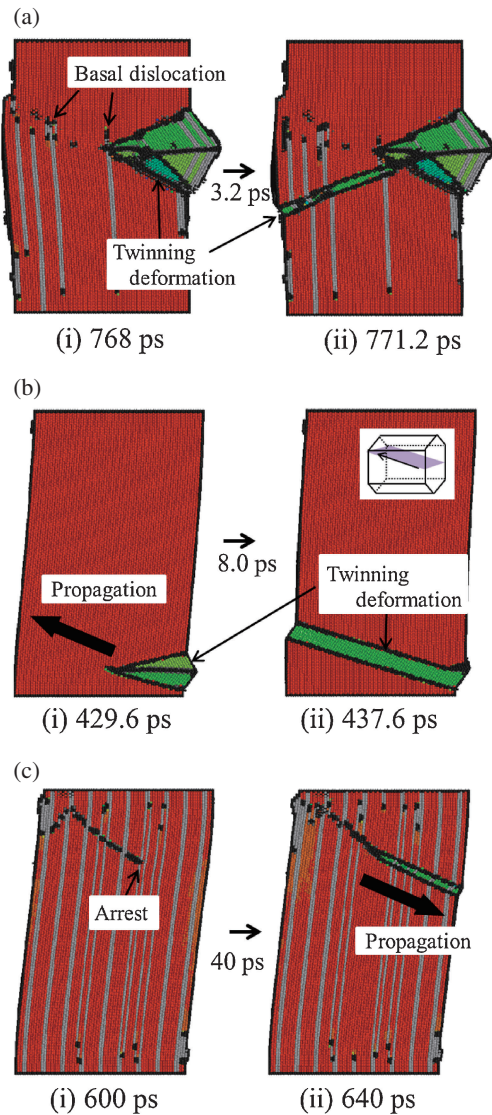


Fig. 5 Structure change during twinning deformation: (a) hcp structure deformed under $\alpha = 0$ and $\dot{\epsilon}^{eq} = 10^8 \text{ s}^{-1}$, (b) hcp structure deformed under $\alpha = 4$ and $\dot{\epsilon}^{eq} = 10^8 \text{ s}^{-1}$, (c) LPSO structure with 24R stacking deformed under $\alpha = 4$ and $\dot{\epsilon}^{eq} = 10^8 \text{ s}^{-1}$.

Fig. 4). The twinning boundary was $\{11\bar{2}1\}$ and the twinning direction was $(1/3) \langle \bar{1}\bar{1}26 \rangle$. This twinning boundary and direction agrees with the recent report by Inui *et al.*²⁶⁾

3.3 Deformation by non-basal dislocations

Deformation by non-basal dislocations was observed in LPSO structures deformed under pure compression ($\alpha = 0$) except when they deformed by twinning (i.e., 10H, 14H and 24R stacking deformed under $\dot{\epsilon}^{eq} = 10^9$, and 10H, 18R and 14H stacking deformed under $\dot{\epsilon}^{eq} = 10^8$). The compressive stress in these cases is higher than that in the HCP structure that underwent twinning deformation (Fig. 3(a)). Figure 6 shows the typical deformation process by non-basal dislocations observed in LPSO structures with 10H stacking deformed under $\alpha = 0$ and $\dot{\epsilon}^{eq} = 10^8 \text{ s}^{-1}$. The deformation was mainly caused by prismatic- $\langle a \rangle$ dislocations ($\{10\bar{1}0\}\langle \bar{1}210 \rangle$) (see Fig. 6(i)). Although the resolved shear stress along the basal-slip direction is ideally zero, some basal dislocations ($(0001) \langle 11\bar{2}0 \rangle$), which are decomposed into

partial dislocations, appeared (Figs. 6(ii), 6(iii) and 6(iv)). These basal dislocations were mainly generated through the cross slip of the screw component of the prismatic- $\langle a \rangle$ dislocation as shown in Fig. 6(ii), and thus those perfect dislocations includes screw component. The migration of screw component of the prismatic- $\langle a \rangle$ dislocation was frequently arrested when they cross FCC-structured layers. This trapping of dislocation migration at FCC-structured layers probably enhances the cross slip of prismatic- $\langle a \rangle$ dislocation to the basal plane.

3.4 Kinking deformation

Kinking deformation, in which many basal dislocations nucleate and those dislocations originate the compressive deformation by generating a misorientation angle by arranging in a line, was observed in LPSO structures deformed under $\alpha = 4$ except when they deformed by twinning deformation (i.e., 10H, 18R and 24R stacking deformed under $\dot{\epsilon}^{eq} = 10^9$, and 10H, 18R and 14H stacking deformed under $\dot{\epsilon}^{eq} = 10^8$). For these cases, as shown in Fig. 3(c), the compressive stress after yielding is at a much higher level compared with the cases of structures deformed by other deformation modes (LPSO structures with 24R stacking, HCP structures, and FCC structures). Figure 7 shows the typical kinking-deformation process observed in LPSO structures with 10H stacking deformed under $\alpha = 4$ and $\dot{\epsilon}^{eq} = 10^8 \text{ s}^{-1}$. At the initial stage of the deformation, nucleations of some partial dislocations on basal plane are observed (Fig. 7(i)). We confirmed that these dislocations were generated from free surfaces normal to the z -axis by forming arc-like loops. It is thought that these basal slips at the beginning of deformation were simply activated by the high resolved shear stress because the shear stress becomes very high under $\alpha = 4$. After the compressive stress sufficiently increased, the non-basal slip caused by first-order pyramidal- $\langle c + a \rangle$ dislocations ($\{10\bar{1}1\}\langle \bar{1}\bar{1}23 \rangle$) was observed (Figs. 7(i) and 7(ii)). Since the pyramidal dislocation migrates across FCC- and HCP-structured layers, it shows stop-and-go motion and the migration velocity is slow. Interestingly, the pyramidal dislocation disarranges the stacking of LPSO structures and leaves behind many lattice defects in a line (Figs. 7(i) and 7(ii)). Furthermore, those lattice defects migrate on the basal plane and split into two partial dislocations moving in opposite directions (Figs. 7(ii) and 7(iii)). Hence, although FCC-structured layers inhibit non-basal slips, once the pyramidal- $\langle c + a \rangle$ dislocation moves, it activates numerous basal slips. Then, many basal dislocations are aligned along the upper and lower boundaries, and they generated a misorientation angle as if the edge dislocations formed tilted grain boundaries. Finally, the misorientation angle originates the compressive deformation. We also observed some prismatic- $\langle a \rangle$ dislocations, and cross slip to the basal plane, similar to the compressive deformation shown in the previous section. It has been reported that dislocations associated with a kink boundary in Ti_3SiC_2 deformed at room temperature also have both edge and screw components.²⁷⁾

As shown in Fig. 3(b), the shear stress is very small except at the beginning of the deformation. This result indicates that basal dislocations nucleate easily from lattice defects

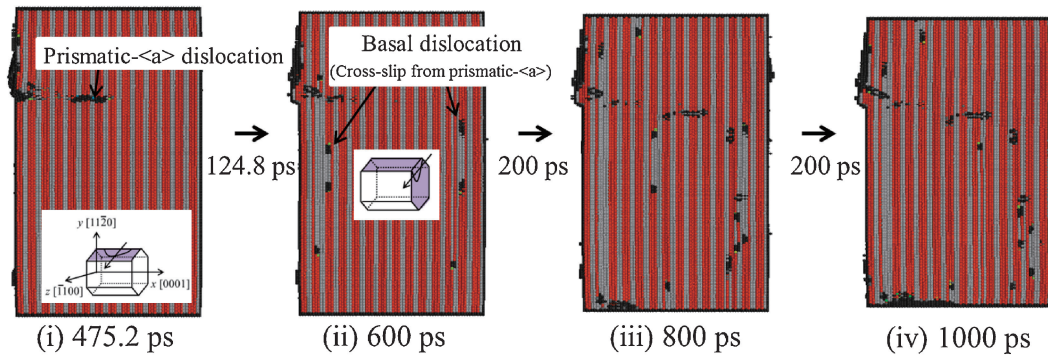


Fig. 6 Deformation process by non-basal dislocations (LPSO structure with 10H stacking deformed under $\alpha = 0$ and $\dot{\epsilon}^{eq} = 10^8 \text{ s}^{-1}$).

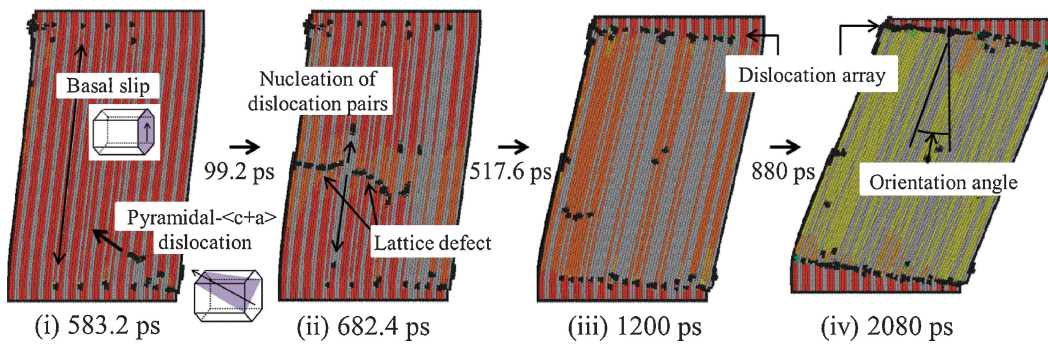


Fig. 7 Structure change during kinking deformation (LPSO structure with 10H stacking deformed under $\alpha = 4$ and $\dot{\epsilon}^{eq} = 10^8 \text{ s}^{-1}$).

generated by the non-basal dislocations. Furthermore, the serration in the compressive stress–strain curves (Fig. 3(c)) generally corresponds to the intermittent migration of the pyramidal dislocation and nucleation of basal dislocations, and the gradual decrease of compressive stress corresponds to the increase in the misorientation angle at kink boundaries.

We also performed deformation analyses for quasi three-dimensional models as a preliminary study; the models have a plate shape with a small thickness ($\approx 1.7 \text{ nm}$), and a periodic boundary condition is applied along the z -axis. Out-of-plane deformation cannot operate under this boundary condition, and we only observed twinning deformation in both HCP and LPSO structures. This result indicates the importance of non-basal slips for the kinking deformation of LPSO structures.

4. Conclusion

We analyzed the deformation behavior of the LPSO phases with different stacking sequences (10H, 18R, 14H and 24R) using MD simulations. We modeled LPSO structures by single element composition in which atoms interact via the SLJ potential. To highlight the specific deformation behavior of the LPSO phases, we also performed deformation analyses of HCP and FCC structures.

- (1) An LPSO phase with a shorter stacking sequence tends to exhibit a higher compressive maximum stress, because FCC-structured layers inhibit twinning deformations and non-basal slips.
- (2) The HCP structure deforms by the catastrophic propagation of twinning deformation, and the stress sharply decreases to small magnitude under all

deformation conditions analyzed herein. Twinning deformation is also observed in deformed LPSO structures under some deformation conditions. The leading edge of twinning deformation is frequently arrested at FCC-structured layers, and the propagation in LPSO structures become much slower than that in the HCP structure.

- (3) LPSO structures are mainly deformed by prismatic-⟨a⟩ dislocations under the pure compression. The prismatic-⟨a⟩ dislocations are frequently arrested when they cross FCC-structured layers, and a lot of cross slips of the screw component of the prismatic-⟨a⟩ dislocations to the basal plane occur.
- (4) Kinking deformation is observed for LPSO structures when both compression and shear deformation are loaded. It is shown that first-order pyramidal-⟨c + a⟩ dislocations disarrange the stacking of LPSO structures and leave behind numerous lattice defects arranged in a line. Those lattice defects activate many basal slips. Finally, basal dislocations align and generate a misorientation angle, and this angle starts the compressive deformation. Some prismatic-⟨a⟩ dislocations and cross slip to the basal plane are also observed. These results suggest the importance of non-basal slips for the kinking deformation of LPSO structures.

Acknowledgments

This work was supported by a Grant-in-Aid for Scientific Research on Innovative Areas “Synchronized Long-Period Stacking Ordered Structure” from the Ministry of Education, Culture, Sports, Science and Technology (MEXT) of Japan.

REFERENCES

- 1) Y. Kawamura, K. Hayashi, A. Inoue and T. Masumoto: *Mater. Trans.* **42** (2001) 1172–1176.
- 2) E. Abe, Y. Kawamura, K. Hayashi and A. Inoue: *Acta Mater.* **50** (2002) 3845–3857.
- 3) M. Yamasaki, M. Sasaki, M. Nishijima, K. Hiraga and Y. Kawamura: *Acta Mater.* **55** (2007) 6798–6805.
- 4) Y. Kawamura and M. Yamasaki: *Mater. Trans.* **48** (2007) 2986–2992.
- 5) M. Yamasaki, K. Hashimoto, K. Hagihara and Y. Kawamura: *Acta Mater.* **59** (2011) 3646–3658.
- 6) T. Itoi, K. Takahashi, H. Moriyama and M. Hirohashi: *Scr. Mater.* **59** (2008) 1155–1158.
- 7) K. Hagihara, N. Yokotani and Y. Umakoshi: *Intermetallics* **18** (2010) 267–276.
- 8) X. H. Shao, Z. Q. Yang and X. L. Ma: *Acta Mater.* **58** (2010) 4760–4771.
- 9) J. B. Hess and C. S. Barrett: *Trans. Am. Inst. Min. Metall. Eng.* **185** (1949) 599–606.
- 10) M. Matsuda, S. Ii, Y. Kawamura, Y. Ikuhara and M. Nishida: *Mater. Sci. Eng. A* **393** (2005) 269–274.
- 11) E. Abe, A. Ono, T. Itoi, M. Yamasaki and Y. Kawamura: *Philos. Mag. Lett.* **91** (2011) 690–696.
- 12) H. Yokobayashi, K. Kishida, H. Inui, M. Yamasaki and Y. Kawamura: *Acta Mater.* **59** (2011) 7287–7299.
- 13) D. Egusa and E. Abe: *Acta Mater.* **60** (2012) 166–178.
- 14) K. Kishida, H. Yokobayashi, H. Inui, M. Yamasaki and Y. Kawamura: *Intermetallics* **31** (2012) 55–64.
- 15) D. Y. Sun, M. I. Mendelev, C. A. Becker, K. Kubin, T. Haxhimali, M. Asta, J. J. Hoyt, A. Karma and D. J. Srolovitz: *Phys. Rev. B* **73** (2006) 024116.
- 16) R. Pasionot and E. J. Savino: *Phys. Rev. B* **45** (1992) 12704–12710.
- 17) X. Y. Liu, J. B. Adams, F. Ercolessi and J. A. Moriarty: *Model. Simul. Mater. Sci. Eng.* **4** (1996) 293–303.
- 18) M. I. Baskes and R. A. Johnson: *Model. Simul. Mater. Sci. Eng.* **2** (1994) 147–163.
- 19) X. W. Zhou, R. A. Johnson and H. N. G. Wadley: *Phys. Rev. B* **69** (2004) 144113.
- 20) J. A. Yasi, T. Nogaret, D. R. Trinkle, Y. Qi, L. G. Hector, Jr. and W. A. Curtin: *Model. Simul. Mater. Sci. Eng.* **17** (2009) 055012.
- 21) R. Matsumoto and N. Miyazaki: *Scr. Mater.* **59** (2008) 107–110.
- 22) R. Matsumoto and M. Nakagaki: *Model. Simul. Mater. Sci. Eng.* **14** (2006) S47–S54.
- 23) Y. Minonishi, S. Ishioka, M. Koiwa, S. Morozumi and M. Yamaguchi: *Philos. Mag. A* **43** (1981) 1017–1026.
- 24) S. Ando, T. Gotoh and H. Tonda: *Metall. Mater. Trans. A* **33** (2005) 823–829.
- 25) J. D. Honeycutt and H. C. Andersen: *J. Phys. Chem.* **91** (1987) 4950–4963.
- 26) Private communication with H. Inui.
- 27) L. Farber, I. Levin and M. W. Barsoum: *Philos. Mag. Lett.* **79** (1999) 163–170.